Mixed-mode Crack-tip Deformations Studied Using a Modified Flexural Specimen and Coherent Gradient Sensing

by S. Ramaswamy, H.V. Tippur and L. Xu

ABSTRACT—An optical mapping of deformation fields and evaluation of fracture parameters near mixed-mode cracks in homogeneous specimens under elastostatic conditions is undertaken. A modified edge notched flexural geometry is used in the study and its ability in providing a relatively wide range of mode mixities is demonstrated. A full-field, optical shearing interferometry called 'coherent gradient sensing' (CGS) is used in the study. Crack-tip parameters such as stress-intensity factors, mode mixity and energy-release rate are measured from the interference patterns. The patterns are analyzed using Williams' mixed-mode, asymptotic expansion field. An expression for energy-release rate for the specimen is also derived using beam theory. The theoretical stress-intensity factors are then obtained using a mode-partitioning method based on moment decomposition. Experimental measurements and theoretical predictions are found to be in good agreement. Limitations of the mode-partitioning method used in the investigation are also pointed out.

Introduction

Practical plane fracture problems often belong to a mixed-mode category. Over the years, several mixed-mode fracture studies on homogeneous materials have been reported.[1-9] In recent years, a renewed interest in mixed-mode fracture research is seen. This is because advanced materials are often seen to fail through mixed-mode fracture. Crack growth along weak interfaces in composite materials is also shown to be inherently mixed-mode[10-14] and is one of the main contributing factors to composite-material fracture.

The following are some of the recent mixed-mode fracture-mechanics reports. Atkinson, *et al.*[1] have proposed a cracked Brazilian disk for mixed-mode fracture study. Richard[2] has reported experimental results and numerical comparisons for a compact tension-shear specimen. Mahajan and Ravi-Chandar[3] have used a similar geometry for determining mixed-mode stress-intensity factors using the method of caustics. They have also measured toughness characteristics for PMMA and Homalite-100. Royer[4] has used a Y-shaped specimen in his investigation to plot failure envelopes under mixed-mode loading. The crack kinking directions are also studied in this investigation. Singh and Shetty[5] have used the Brazilian disk geometry to obtain the fracture toughness of ceramics under mixed-mode loadings. Williams[6] has provided analytical solutions for a family of beam geometries through energy-release-rate calculations. Mason *et al.*[7] have studied dynamic, mixed-mode, K-dominant crack-tip fields. Suresh *et al.*[8] have reported experimental and numerical results on the mixed-mode fracture toughness of ceramic materials.

A flexural fracture specimen is preferable in mixed-mode studies due to the simplicity of loading and compactness it offers. These features make beam specimens popular in composite-material fracture testing as well. In this paper, the feasibility of using a transversely cracked beam specimen (Type-A) for mixed-mode crack-tip field study is demonstrated. The specimen is useful for bimaterial fracture toughness testing[15] as well. The single crack-tip configuration of the specimen greatly reduces restrictions in terms of loading symmetry and thus provides greater experimental consistency. A relatively new, wavefront shearing interferometry, coherent gradient sensing (CGS), is extended to the measurement of mixed-mode crack-tip fields in the specimen (see next section). The optical measurements are used in evaluating mixed-mode crack-tip parameters (see 'Mixed-mode Fracture Experiments' below). Due to the finite size of the specimens, higher order nonsingular deformations generally influence the crack-tip fields. Hence, the assumptions of K dominance are relaxed and higher order terms are included in the analysis of CGS patterns. It is demonstrated that CGS fringes, when used in conjunction with Williams'

S. Ramaswamy is Graduate Student, H.V. Tippur is Assistant Professor, and L. Xu is Graduate Student, Department of Mechanical Engineering, Auburn University, Auburn, AL 36849

Original manuscript submitted: August 1992. Final manuscript received: April 22, 1993.

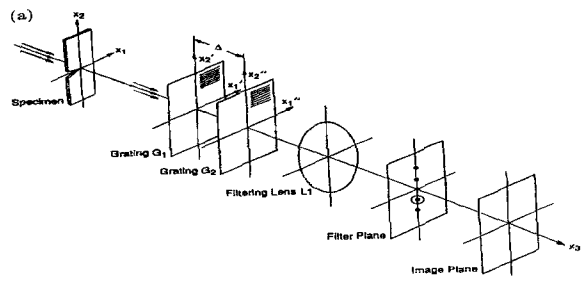

Fig. 1—(a) Schematic of the experimental setup for transmission CGS

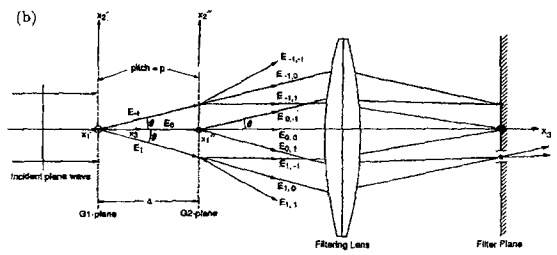

Fig. 1—(b) Working principle of CGS

mixed-mode asymptotic crack-tip fields,[16] provide accurate measurement of crack-tip parameters. Also, using beam theory, expressions for crack-tip energy-release rate and stress-intensity factors are explicitly derived and experimental measurements are compared with the theoretical counterparts.

The paper also points out certain limitations of the mode-partitioning method reported in the literature.[6] This is an outcome of the optical investigation on an alternative modified three-point-bending specimen (Type-B), proposed in the literature[6] for mixed-mode fracture testing based on theoretical calculations. It is shown that the mode-partitioning method which uses a moment decomposition technique is limited to flexural specimens with a geometrical parameter $\xi = 0.5$.

Coherent Gradient Sensing (CGS)

CGS is a wave-front shearing interferometry which can be used to map gradients of deformations near cracks.[17,18] It provides full-field information, offers real-time capability and the sensitivity of measurement is easily controllable. The method is relatively insensitive to random vibrations and rigid motions as well. Also, it can be used with opaque (reflection mode) as well as transparent solids (transmission mode).

The schematic for transmission CGS is shown in Fig. 1(a). A collimated laser beam is transmitted through a transparent fracture specimen. In the vicinity of a deformed crack, nonuniform stress fields exist and hence the incident planar wavefront is perturbed upon propagation through the crack-tip region. One could view the perturbed wavefront to be made of several locally planar wavefronts with propagation vectors oriented in different directions. If $\beta_1(x_1, x_2)$, $\beta_2(x_1, x_2)$ and $\beta_3(x_1, x_2)$ denote the direction cosines of the local propagation vector **d**, then

$$\mathbf{d} = \beta_i \, \mathbf{e}_i \qquad i = 1, 2, 3 \tag{1}$$

where $\mathbf{e}_i$ represent unit normals along Cartesian coordinates. The object wavefront, which carries information about crack-tip deformations, subsequently undergoes a series of diffractions as it propagates through two identical high-density Ronchi gratings, G_1 and G_2 (grating pitch p), which are spatially separated by a distance Δ along the optical axis [Fig. 1(b)]. The gratings are chromium-on-glass master gratings with antireflection coatings and they have a nearly square wave transmission profile. From Fig. 1(b), it is clear that the diffracted wavefronts $E_{(0,1)}$ and $E_{(1,0)}$ are spatially sheared versions of the object wavefront. The path difference between these two wavefronts is a function of the local direction cosines of the object wavefront. Also, because the propagation directions of $E_{(0,1)}$ and $E_{(1,0)}$ are the same, they will come to focus at a common point on the back focal plane of the filtering lens. The spatial frequency content of the object wavefront is filtered at the filtering plane and the interference patterns are photographed on the image plane.

Through a first-order diffraction analysis, Tippur *et al.*[17] and Tippur[18] have related the interference patterns to the direction cosines, β_1 and β_2, of the object wavefront as

$$\beta_\alpha = \frac{n_\alpha p}{\Delta}$$

$$\alpha = 1, 2 \qquad n_\alpha = 0, \pm 1, \pm 2, \ldots \tag{2}$$

where n_α represent fringe orders. The above relationship is valid for small angular deflections of the light rays ($\beta_3 \approx 1$). The direction cosines can be further related to the deformation field under a plane-stress assumption. A detailed analysis has shown that, for transmission CGS, the following governing relations between mechanical fields and optical patterns exist:

$$\beta_\alpha = cB \frac{\partial(\sigma_{11} + \sigma_{22})}{\partial x_\alpha} = \frac{n_\alpha p}{\Delta} \qquad \alpha = 1, 2 \tag{3}$$

where σ_{11}, σ_{22} are the through-the-thickness average of normal stress components, c is the elasto-optical constant (see Appendix A) for the material and B is the undeformed plate thickness.

Mixed-mode Fracture Experiments

Test Specimens and Optical Measurements

Type-A specimens are made from commercially available PMMA sheets of 9-mm nominal thickness (manufactured by CYRO Industries, Mt. Arlington, NJ). The

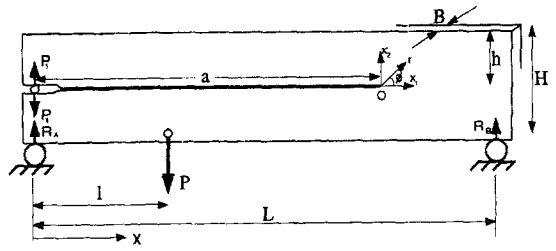

Fig. 2—Transversely cracked beam specimen (Type-A)

specimen geometry and the loading configuration is shown in Fig. 2. A 0.5-mm thick band saw is used to cut transverse slits of different lengths in these specimens. Sufficient care is exercised during cutting in order to minimize residual stresses along the crack flanks and at the crack tip. The cracked edge of the specimen is further notched to a depth of 12.5 mm to produce a slot of width of 6.25 mm. A matching pin is housed in this slot during the test. When the specimen is loaded, the pin induces a reactive force P_1 between the upper and lower arms of the beam. A loose hole of 6.25-mm diameter is drilled in the lower arm for the purpose of applying the load P. Six different crack length (a) to loading distance (l) ratios, namely (a/l) = 1.39, 1.65, 1.91, 2.15, 2.41 and 2.51, are studied. The height of the beam is H = 75 mm and the span of the beam L = 330 mm. The ratio $\xi = (h/H) = 0.5$ in each case.

The specimen is loaded using a plunger which is activated by a hydraulic pump. A 0-3000-lb load cell is used for measuring the applied load P. The load cell is included in the setup in such a way that one end of it is attached to the loading end of the plunger while its other end is connected to a loading fork. The fork forms a pin joint with the specimen and applies the load P to the specimen.

Transmission CGS is used in the present investigation. A collimated laser beam of diameter 50 mm is centered around the crack tip and transmitted through the specimen. The object wavefront undergoes a series of diffractions as it propagates through line gratings G_1 and G_2. The pitch of the line gratings, p, is 0.025 mm and the separation distance between gratings, Δ, is 39 mm. The resulting diffracted wavefronts are brought to focus by the filtering lens. A series of discrete diffraction spots are visible on the filtering plane. A filtering aperture, placed at the back focal plane of the lens, filters either the +1 or -1 diffraction orders. The resulting interference patterns are photographed at the image plane. Note that the imaging system, made of the filtering lens and the camera back, is focussed on the object plane. Typical fringe patterns around the crack tip for three (a/l) ratios when the grating lines are perpendicular to the x_1 axis are shown in Figs. 3(a)-(c). In regions around the crack tip, where plane stress is a good approximation, these fringes represent contours of $cB\dfrac{\partial(\sigma_{11}+\sigma_{22})}{\partial x_1}$, where σ_{11} and σ_{22} are the thickness averages of the normal stress components. The sensitivity of measurement is 6.4×10^{-4} radians per fringe. It should be noted in these patterns that the fringe lobes are asymmetric about the crack, unlike in pure mode-I cases,[17] and thus qualitatively suggest a mixed-mode crack-tip deformation. Moreover, the fringe lobes rotate as (a/l) is varied, indicating changing mode mixity.

Crack-tip Fields

The method of transmission CGS provides gradients of $(\sigma_{11} + \sigma_{22})$ with respect to the x_1 or x_2 coordinate. The measurements performed in this work are restricted to the x_1 gradients of $(\sigma_{11} + \sigma_{22})$ only. Following Williams,[16] for a semi-infinite mixed-mode crack in an infinite elastic sheet,

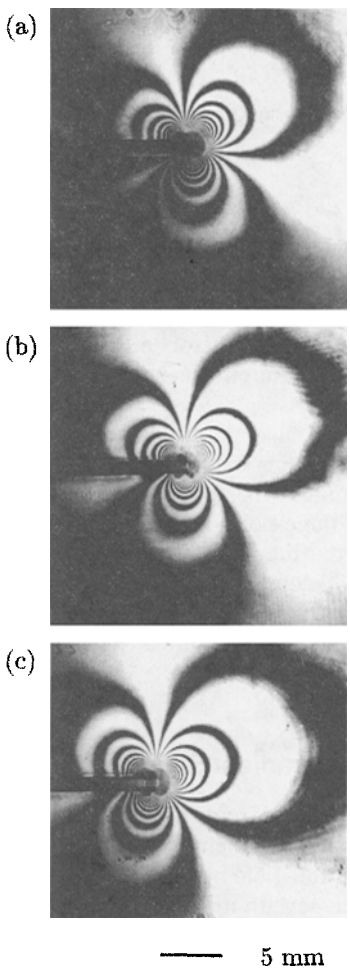

Fig. 3—Transmission CGS fringes representing contours of $\dfrac{\partial(\sigma_{11}+\sigma_{22})}{\partial x_1}$ for Type-A specimens: (a) (a/l) = 1.39, (b) (a/l) = 1.91, and (c) (a/l) = 2.41

$$\frac{\partial(\sigma_{11}+\sigma_{22})}{\partial x_1} = \sum_{N=1}^{\infty}\left(\frac{N}{2}-1\right) r^{\left(\frac{N}{2}-2\right)} \left[A_N \cos\left(\frac{N}{2}-2\right)\phi + B_N \sin\left(\frac{N}{2}-2\right)\phi \right] \quad (4)$$

Here, the coefficients A_N and B_N are the undetermined constants of the series. Now, combining the above with eq (3) we have

$$cB\frac{\partial(\sigma_{11}+\sigma_{22})}{\partial x_1} = cB\sum_{N=1}^{\infty}\left(\frac{N}{2}-1\right) r^{\left(\frac{N}{2}-2\right)} \left[A_N \cos\left(\frac{N}{2}-2\right)\phi + B_N \sin\left(\frac{N}{2}-2\right)\phi \right] = \frac{n_1 p}{\Delta} \quad (5)$$

where c is the elasto-optic constant (the experimental determination of c for the model material is described in Appendix A) and n_1 ($=0, \pm1, \pm2, \ldots$) represent fringe orders. Here, A_1 and B_1 are proportional to stress-intensity factors, K_I and K_{II} respectively, and $A_2, \ldots, A_N, B_2, \ldots, B_N$ are the constant coefficients of higher order terms. Also, note that the term corresponding to $N = 2$, known as the 'T-term' in the fracture-mechanics community, is identically zero and does not contribute to the formation of CGS fringes.

Now, a K-dominant field can be defined as the one in which the contribution from the higher order terms is negligible when compared to the first term ($N = 1$). Thus, for K dominance, eq (5) reduces to

$$\frac{cBr^{-3/2}}{\sqrt{2\pi}}\left[-K_I \cos(3\phi/2) + K_{II}\sin(3\phi/2)\right] = \frac{n_1 p}{\Delta} \quad (6)$$

Measurement of K_I and K_{II} from Fringe Patterns

It is evident from eq (6) that, for CGS patterns, one of the necessary conditions for K dominance to prevail in the crack-tip vicinity is that $(n_1 r^{3/2})$ remain constant for different ϕ when plotted against (r/B). These constant values could be different for different ϕ. This condition alone, however, is insufficient to conclude K dominance. It is also necessary that the constants so obtained along different ϕ, when solved simultaneously, produce K_I, and K_{II} which agree with the corresponding ones from boundary measurements. To test the above, fringe location (r) and fringe order (n_1) data are measured all around the crack tip (-150 deg $< \phi <$ 150 deg) where fringes unambiguously intersect with radial lines drawn from the crack tip along different ϕ. A typical plot of $(n_1 r^{3/2})$ versus (r/B) for different ϕ is shown in Fig. 4(a) for the case of $(a/l) = 1.91$. Clearly, $n_1 r^{3/2}$ is not a constant over any sizeable radial distance near the crack tip suggesting a general lack of K dominance.

The absence of K dominance in the region within $(r/B) = 0.5$ observed in Fig. 4(a) can be attributed to three-dimensional deformations in the immediate vicinity of the crack tip (Rosakis and Ravi-Chandar[19]) in finite-thickness specimens. Three-dimensional effects, generally prevent the data from within $(r/B) = 0.5$ from being analyzable using two-dimensional descriptions. For mode-I cracks, however, both optical data and finite-element results[17] have revealed that there are sectors or regions in the crack-tip vicinity where three-dimensional effects are minimal and the two-dimensional singular term is dominant. The data in these regions, although well within the $(r/B)=0.5$ limit, can be well described by the K-dominant field and thus suggest the validity mode-I fracture is linked to critical K_I. Similar information for mixed-mode cracks is not available at the moment. However, it is quite predictable that such regions also exist in the mixed-mode crack-tip vicinity and the failure process is dependent on the critical values of K_I and K_{II}.

The lack of sizeable K-dominant regions beyond $(r/B) = 0.5$ in Fig. 4(a), could be attributed to the influence of higher order terms on the crack-tip fields. Nonsingular contributions generally influence the K-dominant field at these distances. Moreover, the proximity of the boundaries in finite-size specimens contribute to this to a greater extent. Thus, by using higher order terms in additional to the K-dominant terms in the analysis, it is possible to delineate the far-field effects from the dominant singular terms. The values of stress-intensity factors thus obtained, if in agreement with boundary measurements, are acceptable as reliable fracture parameters. Also, measuring K_I and K_{II} from the data obtained from a non-K-dominant region is again based on the assumption that stress-intensity factors can satisfactorily describe the fracture process close to the crack tip.

To extract, stress-intensity factors from the fringe data in regions beyond $(r/B)=0.5$, a multiparameter least-squares data analysis is used. Denoting the right-hand sides of eq (5) by Y and F, respectively, a function $\Phi(A_1, A_2 \ldots, A_N, B_1, B_2, \ldots B_N; r, \phi)$ is defined as

$$\Phi = \sum_{i=1}^{M} [\, Y_i - F_i \,]^2 \quad (7)$$

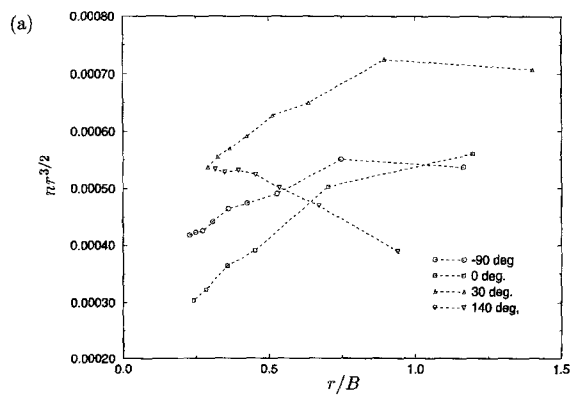

Fig. 4—(a) Variation of $(n_1 r^{3/2})$ with normalized radial distance

where M is the total number of data points used in the analysis. In the curve-fitting procedure, Φ is minimized with respect to $A_1,...A_N$, $B_1,...B_N$. The values of $\sqrt{\frac{\pi}{2}}\,A_1$ and $\sqrt{\frac{\pi}{2}}\,B_1$ corresponding to the least-squares data fit are experimentally determined stress-intensity factors and are denoted by K_I^{exp} and K_{II}^{exp}.

Each fringe pattern is first analyzed under the assumption of K-dominance [N = 1 in eq (6)]. A typical result shown in Fig. 4(b) for a (a/l) = 1.91. The disagreement between the experimental data and the least-squares fit is clearly evident and it suggests a need for including higher order terms in the least-squares analysis. However, the exact number of terms required to achieve a least-squares fit which conforms well with the optical data is unknown *a priori*. This problem is solved by inclusion of higher order terms in the least-squares data analysis to improve the agreement between the fit and experimental data. However, the inclusion of higher order terms beyond a certain number tends to produce larger disagreement between the fit and the data. This may be attributed to the inherent 'noise' in the digitized experimental data due to errors associated with locating fringe centers. However, there exists an optimum number of terms in the expansion which will provide the 'best' fit to the digitized data. Any number of terms different from this optimum N would produce larger deviations between the fit and the data. Standard deviation (S) is used as a measure for estimating the optimum number of terms required to obtain the 'best' fit. This is determined by finding the deviation of each data point from the corresponding point on the fit along discrete radial directions as follows

$$S = \frac{1}{(M-1)}\sqrt{\sum_{i=1}^{M}(r^{fit} - r^{exp})_i^2} \tag{8}$$

The value of N is then increased in steps and S is calculated for each value of N. Figure 4(c) shows the 'best' fit for (a/l) = 1.91 wherein the agreement between the measured data and the fit is reasonably good. The broken circle represents the region corresponding to (r/B) = 0.5. The values of stress-intensity factors K_I, K_{II}, standard deviation S and higher order coefficients for (a/l)= 1.91 are tabulated for different values of N in Table 1. From the table, it is evident that as N is increased, the variation of stress-intensity factors is initially noticeable and each attains a stable value as the optimal N is approached. Thus, the values of stress-intensity factors from the 'best' fit also correspond to equilibrium values of the constant coefficients of $r^{-3/2}$.

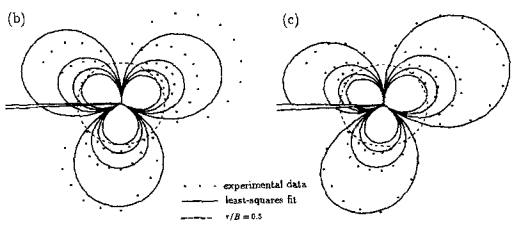

Fig 4—(b) least-square kit for K-dominant terms (N = 1), (c) least-square fit for higher order terms ('best fit'; N = 5), for (a/l) = 1.91

Calculation of K_I^{th}, K_{II}^{th}, G from Beam Analysis

In the following, the expressions for theoretical energy-release rate (G), and hence stress-intensity factors, K_I^{th} and K_{II}^{th}, are derived. Under the action of the load P (Fig. 2), the strain energy, U_S, stored in the beam due to bending is

$$U_S = \int_0^a \frac{[M_u(x)]^2}{2EI_1}dx + \int_0^a \frac{[M_l(x)]^2}{2EI_2}dx + \int_a^L \frac{[M_u(x)+M_l(x)]^2}{2EI_0}dx \tag{9}$$

where, $M_u(x)$ and $M_l(x)$ are the respective moments in the upper and lower arms of the beam at any location x; $I_1 = \frac{1}{12}Bh^3$, $I_2 = \frac{1}{12}B(H-h)^3$ and $I_0 = \frac{1}{12}BH^3$ are the moments of inertia of the cross-sections of the upper arm, the lower arm and the uncracked portion respectively; and E is the Young's modulus of the material. Let $R_A\left[=P\left(1-\frac{l}{L}\right)\right]$ and R_B denote the support reactions. Using Castigliano's principle, it can be shown[16] that the reactive force P_1 between the two arms is

$$P_1 = \frac{P}{2}\left[\frac{3}{2}\left(\frac{l}{a}\right) - \frac{1}{2}\left(\frac{l}{a}\right)^3 - \left(\frac{l}{L}\right)\right]$$

Then, the expression for strain energy becomes

$$U_S = \int_0^a \frac{(P_1 x)^2}{2EI_1}dx + \int_0^a \frac{[(R_A - P_1)x - P\langle x-l\rangle]^2}{2EI_2}dx + \int_a^L \frac{[P_1 x + (R_A - P_1)x - P\langle x-l\rangle]^2}{2EI_0}dx \tag{10}$$

where the discontinuity function $\langle\cdot\rangle$ is defined as $\langle x-l\rangle = (x-l)$ for $x \geq l$ and, $= 0$ otherwise. Thus energy-release rate (G) for the cracked geometry can be expressed as

$$G = \frac{1}{B}\frac{dU_S}{da} = \frac{1}{2B}\left[\frac{M_1^2}{EI_1} + \frac{M_2^2}{EI_2} - \frac{(M_1+M_2)^2}{EI_0}\right] \tag{11}$$

where B is the thickness of the specimen and

$$P_1 a = M_1$$
$$(R_A - P_1)\,a - P\,(a-l) = M_2$$

are the crack-tip moments in the upper and lower arms of the beam. Now, upon defining $I = BH^3/96$ and the height ratio, $\xi = h/H$, the expression for energy-release rate in the homogeneous specimen becomes

TABLE 1—VARIATION OF K_I, K_{II}, HIGHER ORDER TERMS, AND S WITH N FOR $(a/l) = 1.91$

N	S	K_I	K_{II}	$(A_3, B_3), (A_4), (A_5, B_5)...$
1	0.0279	1.03	-0.89	
3	0.0243	0.98	-0.79	(-13.4, 9.1)
4	0.0245	0.91	-0.79	(-30.5, 10.4), (170.2)
5	0.0240	0.85	-0.79	(-29.8, 7.7), (220.8), (-861.2, -486.0)
6	0.0247	0.85	-0.79	(-45.8, 1.6), (676.7), (-6764.0, -2371.7), (33459.0, 6613.0)

Units of K_I and K_{II} are MPa $\sqrt{m}$. Units of: $(\cdot)_3$ is MPa/$\sqrt{m}$; $(\cdot)_4$ is MPa/m, etc. $N = 5$ corresponds to the 'best' least-squares fit.

$$G = \frac{1}{16BEI}\left[\frac{M_1^2}{\xi^3} + \frac{M_2^2}{(1-\xi)^3} - (M_1 + M_2)^2\right] \quad (12)$$

In order to calculate K_I^{th} and K_{II}^{th} from G, a mode-partitioning method outlined by Williams[6] is used. *It should be pointed out, however, that the method is only applicable to the special case of* $\xi = 0.5$. Through optical measurements and finite-element computations it is shown in 'Mode Partitioning: Limitation' below that the generalization of the method for all ξ, as presented in Ref. 6, is incorrect.

The mode-partitioning method is basically a moment-decomposition technique in which the system of moments M_1 and M_2 at the crack tip can be written in terms of M_I and M_{II}, where M_I and M_{II}, respectively, represent the moments responsible for pure mode-I and pure mode-II deformations at the crack tip. This moment decomposition is based on the assumption that the radii of curvature of the upper and lower beams should be equal in magnitude when the crack propagates under pure mode-I or pure mode-II. For pure mode-I deformation, the curvatures of the upper and lower beams have opposite signs, while they are identical for pure mode-II deformation as shown schematically in Fig. 5. Thus it follows that for Type-A specimens $(\xi = 0.5)$, $M_1 = M_I + M_{II}$ and $M_2 = M_{II} - M_I$. After substituting for M_1 and M_2 in eq (12), and grouping the terms involving M_I, and M_{II}, energy-release rate can be expressed as

$$G = \frac{1}{BEI}\left(M_I^2 + \frac{3}{4}M_{II}^2\right) \quad (13)$$

Thus, energy-release rate can be expressed unambiguously in terms of the energy-release rates associated with symmetric deformations $[G_I(M_I)]$ and anti-symmetric deformations $[G_{II}(M_{II})]$ as follows.

$$G_I = \frac{(K_I^{th})^2}{E} = \left(\frac{3P^2l^2}{4B^2Eh^3}\right)\left[1 - \left(\frac{l}{a}\right)^2\right]^{-2} \quad (14)$$

$$G_{II} = \frac{(K_{II}^{th})^2}{E} = \left(\frac{9P^2l^2}{4B^2Eh^3}\right)\left[1 - \left(\frac{a}{L}\right)^2\right]^{-2} \quad (15)$$

From the above equations, K_I^{th} and K_{II}^{th} can be determined.

Results

The results from the experiments and the beam theory for different (a/l) ratios are summarized in Figs. 6 and 7 and Table 2. Figure 6 shows the variations of normalized theoretical and experimental values of K_I and K_{II} with respect to (a/l). The stress-intensity factors are normalized by $\sqrt{K_I^2 + K_{II}^2}$. As noted earlier, the mode-mixity varies with (a/l); while K_I increases with (a/l) and K_{II} decreases. The solid curves in Fig. 6 represent the theoretical prediction, while the triangles and boxes represent the experimental measurements. The experimental results shown correspond to the 'best' least-squares fit. The measurements are in good agreement with the beam model. Figure 7 shows

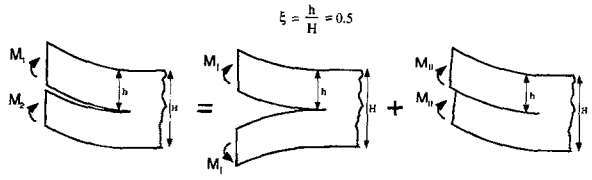

Fig. 5—Mode partitioning by moment decomposition

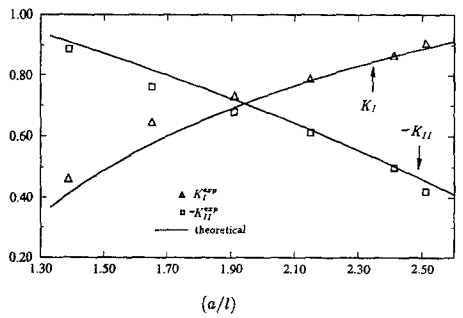

Fig. 6—Variation of normalized mode-I and mode-II stress-intensity factors with normalized crack length (a/l)

TABLE 2—SUMMARY OF MIXED-MODE CRACK-TIP MEASUREMENTS IN TYPE-A SPECIMENS

a/l	P	K_I^{th}	K_{II}^{th}	K_I^{exp}	K_{II}^{exp}	N	$K_I^{exp(b)}$	$K_{II}^{exp(b)}$	$-\psi^{th}$	$-\psi^{exp}$	$-\psi^{exp(b)}$
1.39	786	0.48	-1.02	0.66	-1.30	4	0.60	-1.14	64.8	63.1	62.2
1.65	723	0.64	-0.89	0.84	-1.01	5	0.74	-0.87	54.3	50.3	49.6
1.91	723	0.72	-0.74	1.03	-0.89	5	0.85	-0.79	45.8	40.8	42.9
2.15	723	0.78	-0.60	1.02	-0.74	5	0.83	-0.64	37.6	36.0	37.6
2.41	736	0.84	-0.48	0.97	-0.67	5	0.86	-0.49	29.7	34.6	29.7
2.51	1364	1.18	-0.59	1.16	-0.56	5	1.02	-0.47	26.6	25.8	24.7

$(*)^{exp}$ and $(*)^{exp(b)}$ correspond to the K-dominant field and the asymptotic field cases, respectively, of the experimental results. SIF values are in MPa$\sqrt{m}$, ψ values are in degrees, and P is in Newtons. N corresponds to the optimum value that produces the best least-squares fit.

a plot of the mode mixity parameter, ψ (= $\tan^{-1} K_{II}/K_I$) versus (a/l). The solid line represents theoretical prediction and the circles are the experimental measurements. A fairly wide range of mode mixities, $\psi \approx 20$ deg - 65 deg, obtained suggest the appropriateness of the specimen for mixed-mode fracture studies. Table 2 summarizes all the results for the entire range of (a/l) investigated. The load levels to which the stress-intensity factors correspond are also listed. Two sets of results, namely the K-dominant case (when only the first term in the expansion field is used) and the asymptotic field case (when the optimum number of higher order terms are used) are presented in the table. The corresponding mode-mixity parameters are also listed. Clearly, inclusion of higher order terms improve the agreement between the experimental and theoretical values. On the other hand, there is no appreciable change in the values of the mode-mixity parameter for the K-dominant and the asymptotic field cases. Thus, it suggests that the use of K-dominant field itself may be sufficient in obtaining reasonably accurate estimates of the mode mixity parameter in this specimen geometry. Finally, the agreement between the experimental results and the corresponding theoretical values show the viability of CGS as an effective technique in performing direct mixed-mode crack-tip measurements.

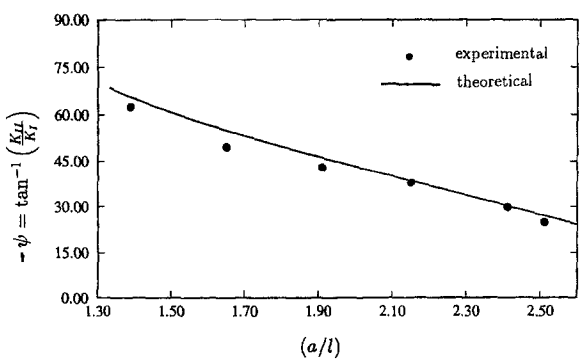

Fig. 7—Variation of mode mixity with normalized crack length

Mode Partitioning: Limitation

As mentioned above, the method of mode partitioning is restricted to the case of $\xi = h/H = 0.5$. When $\xi \neq 0.5$, alternative analyses are necessary to separate symmetric and asymmetric components of the total energy-release rate. On the contrary, the method is suggested for all values of ξ in Ref. 6. This, however, is found incorrect during the course of the present investigation.*

In Ref. 6, an alternative transversely cracked beam specimen (Type-B) [see Fig.(8)] with varying ξ and constant crack length a is proposed for producing a wide range of mode mixities. (It should be noted here that this specimen was considered initially by the authors for studying mixed-mode crack-tip fields and failed to produce a wide range of mode-mixities.) For this specimen, using arguments similar to the ones described in 'Calculation of K_I^{th}, K_{II}^{th}, G from Beam Analysis,' above, the mode mixity ψ is said to vary according to the relationship

$$\psi = \tan^{-1}\left(\frac{\sqrt{3}(1-\xi)^2}{\xi}\right) \tag{16}$$

* *Recently, Williams and his coworkers (Charalambides, et al., Int. J. Fract., 54, 1992) have addressed this by introducing the notion of global and local stress-intensity factors.*

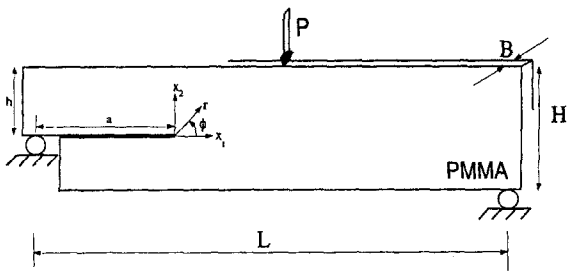

Fig. 8—Mixed-mode fracture specimen (Type-B)

in Ref. 6. Equation (16) is derived by partitioning the moments M_1 and M_2 as $M_1 = M_I + M_{II}$ and $M_2 = q(M_{II} - M_I)$. Here $q = [(1 - \xi)/\xi]^3$ is a scalar obtained by satisfying the equal curvature condition for the upper and the lower arms of the cracked beam. If eq (16) were correct, pure mode-II conditions exist when $\xi \rightarrow 0$ and pure mode-I conditions when $\xi \rightarrow 1$. Optical measurements near the crack tip for three different cases of $\xi = 0.25$, 0.50 and 0.75, however, indicate that the above expression of mode mixity and hence mode-partitioning method is invalid for values of $\xi \neq 0.5$.

Cracked-beam specimens of the above said ξ are made from a PMMA sheet of 9-mm thickness. Other dimensions of the specimen are crack length $a = 90$ mm, span of the beam $L = 330$ mm and height $H = 75$ mm. The beams are loaded as shown in Fig. 8 and the corresponding transmission CGS fringes are shown in Fig. 9. As it can be seen, the fringe rotation, a qualitative measure of changing mode mixity, is approximately the same for all three values of ξ. To measure crack-tip parameters K_I^{exp} and K_{II}^{exp}, the fringe patterns are analyzed using the procedure described in 'Measurement of K_I and K_{II} from Fringe Patterns.' Also, two-dimensional finite-element computations corresponding to the different ξ are performed using ALGOR FEA software. The path independent J integral[20] near the crack tip is evaluated for each case. An example of the near-tip finite-element mesh and the corresponding path of integration is shown in Fig. 10.

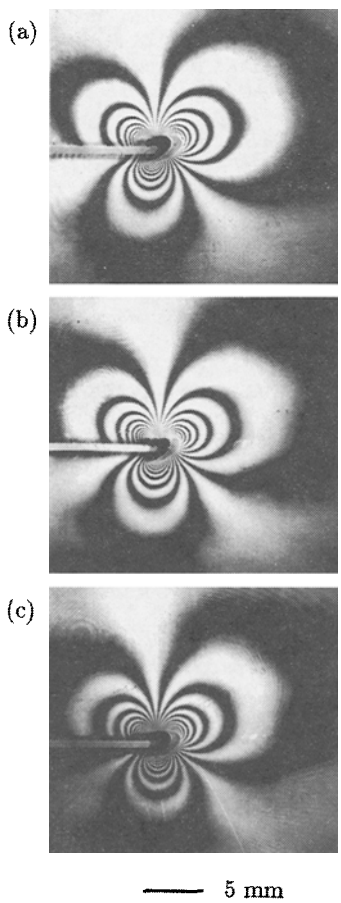

Fig. 9—Transmission CGS fringes representing contours of $\frac{\partial(\sigma_{11}+\sigma_{22})}{\partial x_1}$ for Type-B specimen with (a) $\xi = 0.25$, (b) $\xi = 0.5$, (c) $\xi = 0.75$

For quasi-static problems, for a crack extension in the x_α direction, the J integral is given by

$$J_\alpha = \int_\Gamma \left[W_e l_\alpha - T_i \frac{\partial u_i}{\partial x_\alpha} \right] d\Gamma \qquad \alpha = 1, 2, \quad i = 1, 2 \tag{17}$$

where Γ is an arbitrary closed path surrounding the crack tip, W_e is the strain-energy density, u_i denotes the in-plane displacement components, and T_i represents the traction components ($\sigma_{ij} l_j$, l_j are the direction cosines). By expressing the crack-tip stress, strain and displacement fields as sums of symmetric and antisymmetric components, Kishimoto, *et al.*[21] have shown that for a mixed-mode (mode-I + mode-II) crack tip, J_I, and J_{II}, symmetric and antisymmetric components of J_1 respectively, may be calculated. They are further related to the local crack-tip stress-intensity factors as follows.

$$J_I = \frac{\kappa + 1}{8\mu} K_I^2 \tag{18}$$

$$J_{II} = \frac{\kappa + 1}{8\mu} K_{II}^2 \tag{19}$$

where $\kappa = (3 - \nu)/(1 + \nu)$ for plane stress, μ is the shear modulus and $J_1 = J_I + J_{II}$. From the above equations, the numerical values of stress-intensity factors, K_I^{FEA} and K_{II}^{FEA}, are found.

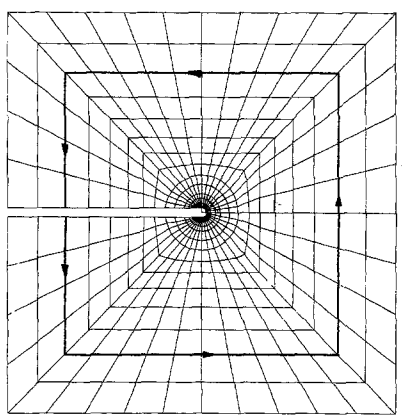

Fig. 10—Finite-element mesh near the crack tip and integration path

TABLE 3—LIMITATION OF MODE-PARTITIONING METHOD DEMONSTRATED USING TYPE-B SPECIMEN

ξ	P	$K_I^{exp(b)}$	$K_{II}^{exp(b)}$	K_I^{FEA}	K_{II}^{FEA}	K_I^{δ}	K_{II}^{δ}
0.25	267	0.88	-0.84	0.86	-1.02	0.05	-0.19
0.50	983	1.10	-0.98	1.00	-0.91	1.20	-1.04
0.75	1826	0.88	-0.97	0.73	-0.83	8.77	-1.27

K_I and K_{II} are in MPa(m).$^{1/2}$ P is in Newtons.

In Table 3 experimental and numerical values of stress-intensity factors along with the values based on eq (16) for the three cases of ξ are compared. The experimental and numerical results for $\xi = 0.25$ and $\xi = 0.75$, while in reasonably good agreement with each other, contrast heavily with the ones based on eq (16). All three values are in fairly good agreement when $\xi = 0.5$. While preparing this report, the authors have come across a review article on mixed-mode fracture of layered materials by Hutchinson and Suo[14] wherein this error in Ref. 6 is also pointed out.

Conclusions

The appropriateness of a transversely cracked beam specimen ($\xi = 0.5$) for mixed-mode fracture studies is examined through direct optical measurements. Optical method of transmission CGS has been used for mapping mixed-mode crack-tip deformations and measuring crack-tip parameters. Because of the finite size of the specimens, nonsingular higher order terms are seen to affect the optical data measured in regions beyond the $r/B = 0.5$ limit. The higher order effects have been successfully delineated from the singular contributions using mixed-mode asymptotic expansion field. A method of extracting K_I and K_{II} using an over-deterministic least-squares analysis is presented. The coefficients of the singular term provide the experimental stress-intensity factors. A relatively wide range of mode mixities have been produced by simply varying the parameter (a/l) in this specimen. Theoretical counterparts are obtained from a flexural analysis by calculating the total energy-release rate followed by mode partitioning. The experimental measurements are found to be in good agreement with the predictions based on beam theory.

Limitations of the mode-partitioning method suggested in the literature are also pointed out in this investigation. It is found that the mode-partitioning method based on moment decomposition is limited to the case of $\xi = 0.5$ and alternative analyses are essential when $\xi \neq 0.5$. This is an outcome of an optical investigation on an alternative three-point-bend fracture specimen which is said to produce a wide range of mode mixities for different ξ ($0 \leq \xi \leq 1$). Finite-element calculations complement experimental measurements in pointing out this limitation.

Acknowledgments

The research is partly supported by NSF Research Initiation Award MSS9109731 to HVT. Equipment assistance by Auburn University through 1991 Research Grant-in-Aid is also gratefully acknowledged.

References

1. Atkinson, C., Smelser, R.E. and Sanchez, J., "Combined Mode Fracture Via the Cracked Brazillian Disk Test," Int. J. Fract. **18**, 279-291 (1982).

2. Richard, H.A., "Some Theoretical and Experimental Aspects of Mixed Mode Fractures," Advances of Fracture Research, Proc. ICF-6, **5**, 3337-3344 (1984).

3. Mahajan, R.V. and Ravi-Chandar, K., "An Experimental Investigation of Mixed-Mode Fracture," Int. J. Fract., **41**, 235-252 (1989).

4. Royer, J., "Study of Pure and Mixed-Mode Fracture of a Brittle Material," EXPERIMENTAL MECHANICS, **28**, 382-387 (1988).

5. Singh, D. and Shetty, D.K., "Fracture Toughness of Polycrystalline Ceramics in Combined Mode I and Mode II Loading," J. Amer. Cer. Soc. **72** (1), 78-84 (1988).

6. Williams, J.G., "On the Calculation of Energy Release Rates for Cracked Laminates," Int. J. Fract. **36**, 101-119 (1988).

7. Mason, J., Lambros, J. and Rosakis, A.J., "The Use of a Coherent Gradient Sensor in Dynamic Mixed-Mode Fracture Mechanics Experiments," Journal of the Mechanics and Physics of Solids, 40, 641-661, (1992).

8. Suresh, S., Shih, C. F., Morrone, A., and O'Dowd, N. P., "Mixed-Mode Fracture Toughness of Ceramic Materials," J. Amer. Cer. Soc., **73** (5), 1257-1267 (1990).

9. Reeder, J.R. and Crews, J.H., "Mixed-Mode Bending Method for Delamination Testing," AIAA J., **28** (7), 1270-1276 (1990).

10. Rice, J.R., "Elastic Fracture Mechanics Concepts for Interface Cracks," J. Appl. Mech., **55**, 98-103 (1988).

11. Charalambides, P.G., Lund, J., Evans, A.G. and McMeeking, R.M., "A Specimen for Determining the Fracture Resistance of Bimaterial Interfaces," J. Appl. Mech., **56**, 77-82 (1989).

12. Tippur, H.V. and Rosakis, A.J., "Quasi-Static and Dynamic Crack Growth Along Bimaterial Interfaces: A Note on Crack Tip Field Measurements Using CGS," EXPERIMENTAL MECHANICS, **31** (3), 243-252 (1991).

13. O'Dowd, N.P., Shih, C.F. and Stout, M.C., "Test Geometries for Measuring Interfacial Fracture Toughness," Int. J. Solids and Structures, **29** (5), 571-589 (1992).

14. Hutchinson, J.W. and Suo, Z., "Mixed Mode Cracking in Layered Materials," Advances in Appl. Mech., **29**, 63-191 (1992).

15. Ramaswamy, S., "An Investigation of Mixed-Mode Fracture in Homogeneous and Bimaterial Solids," MS Thesis, Auburn University, Auburn, AL (1992).

16. Williams, M.L., "On the Stress Distribution at the Base of a Stationary Crack," J. Appl. Mech., **24**, 109-114 (1959).

17. Tippur, H.V., Krishnaswamy, S. and Rosakis, A.J., "Optical Mapping of Crack Tip Deformations Using the Method of Transmission and Reflection Coherent Gradient Sensing: A Study of Crack Tip K-Dominance," Int. J. Fract., **52**, 91-117 (1991).

18. H.V. Tippur, "Coherent Gradient Sensing: A Fourier Optics Analysis and Applications to Fracture," **31** (22), 1428-1439 (1992).

19. Rosakis, A.J. and Ravi-Chandar, K., "On Crack Tip Stress State: An Experimental Evaluation of Three-Dimensional Effects," Int. J. Solids and Structures, **22** (2), 121-134 (1986).

20. Rice, J.R., "A Path Independent Integral and the Approximate Analysis of Strain Concentration by Notches and Cracks," J. Appl. Mech., **35**, 379-386 (1968).

21. Kishimoto, K., Aoki, S. and Sakata, M., "Dynamic Stress Intensity Factors Using J-Integral and Finite Element Method," Eng. Fract. Mech., **13**, 387-394 (1980).

22. Timoshenko, S.P., Theory of Elasticity, McGraw-Hill Publishers (1951).

Appendix A

A calibration experiment to determine the elasto-optic constant c for PMMA is described here. The experiment is carried out using a sheet of 9-mm thick PMMA. The loading device, the rate of loading, the optical setup and the load transducer are all identical to the ones used in mixed-mode fracture study. The sheet is subjected to a line load acting on an edge as shown in Fig. 11(a). Transmission CGS is used to map deformations due to the applied load. The interference patterns represent contours of constant $\frac{\partial(\sigma_{11}+\sigma_{22})}{\partial x_1}$. The fringe pattern, corresponding to a load level of P = 1500 N, is shown in Fig. 11(b).

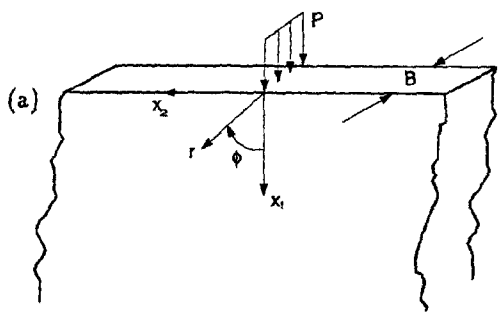

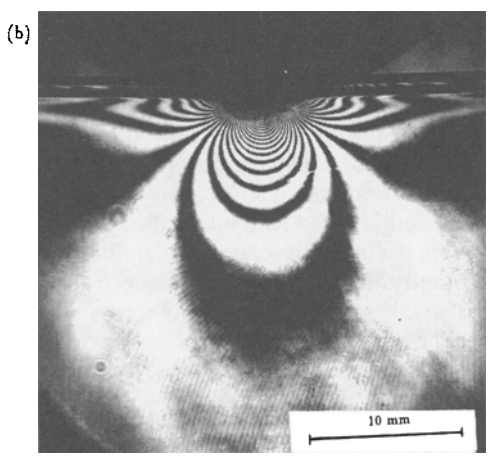

Fig. 11—(a) Line load acting on a half space, (b) contours of $\frac{\partial(\sigma_{11}+\sigma_{22})}{\partial x_1}$ fringes for P = 1500 N

TABLE 4—MATERIAL CALIBRATION

n_1	r/B	$c \times 10^{10}$ (m^2/N)
0.5	1.62	-0.80
1.0	1.20	-0.86
1.5	0.97	-0.87
2.0	0.86	-0.88
2.5	0.77	-0.88
3.0	0.70	-0.87
3.5	0.66	-0.89
4.0	0.62	-0.90

For a half space subjected an edge load, the x_1 gradient of $(\sigma_{11} + \sigma_{22})$ is given by[22]

$$\frac{\partial(\sigma_{11}+\sigma_{22})}{\partial x_1} = \frac{2P\cos 2\phi}{\pi r^2} \tag{20}$$

where r and ϕ are the polar coordinates of a generic point with the point of application of the load as the origin. Using the governing equation for transmission CGS [eq (3)], we can write

$$cB\frac{2P\cos 2\phi}{\pi r^2} = \frac{n_1 p}{\Delta} \tag{21}$$

where n_1(= 0, ±1, ±2,...) represent fringe orders, and c is the elasto-optic constant. Along $\phi = 0$, the fringe orders are negative and the above equation simplifies to

$$c = \frac{n_1 p \pi r^2}{2PB\Delta} \tag{22}$$

The fringe pattern, shown in Fig. 11(b), is digitized along $\phi = 0$ to obtain r corresponding to different fringe orders n_1. The value of c is calculated for each data set using eq (22). A tabulation of c corresponding to different values of (r/B) and n_1 is shown in Table 4. An average value of c = -0.87×10^{-10} m^2/N is used as the elasto-optic constant for the model material. It should also be pointed out that a least-squares analysis using the left-hand side of eq (21) as the fitting function is also used to calculate c. The value of c thus obtained is within three percent of the average value obtained along $\phi = 0$ deg.